



Shape-programmable fluid bubbles for responsive building skins

Raphael Kay^{a,b,c,*}, Kevin Nitièma^c, Charlie Katrycz^a, J. Alstan Jakubiec^{c,d},
Nicholas Hoban^c, Benjamin D. Hatton^a

^a Department of Materials Science and Engineering, University of Toronto, 184 College St, Toronto, Ontario, M5S 3E4, Canada

^b Department of Mechanical and Industrial Engineering, University of Toronto, 5 King's College Road, Toronto, Ontario, M5S 3G8, Canada

^c John H. Daniels Faculty of Architecture, Landscape and Design, University of Toronto, 1 Spadina Crescent, Toronto, Ontario, M5S 2J5, Canada

^d School of the Environment, University of Toronto, 149 College Street, Toronto, Ontario, M5T 1P5, Canada

ARTICLE INFO

Keywords:

Self-assembly
Active optics
Fluidics
Dynamic architecture

ABSTRACT

Building facades that can dynamically absorb light in the visible and near-infrared region of the electromagnetic spectrum enable temporally-programmable optical control and improved building energy-efficiency. Conventional solid-phase chromogenic materials suffer performance limitations that might be addressed by highly-mobile, self-assembling, gas- and liquid-phase alternatives. Here, we introduce a fluidic interface for buildings that can achieve light modulation through reversible injections of air bubbles with self-organizing morphologies. We establish criteria for injection-rate- and flow-field-dependent bubble shape. And we demonstrate experimental control over visible light transmission, near-infrared light transmission, solar heat gain, and indoor temperature, through active modulation of bubble size. Energy models help predict the comparative operational performance of our system, allowing us to couple motion-sensing capabilities with digitally-actuated bubble formation, towards demonstrating the potential for a tunable fluidic mechanism in responsive building design.

1. Introduction

Buildings typically interface with the environment statically [1]. Their outer facades, which regulate the ingress and egress of energy between interior and exterior regimes, are conventionally designed as hybrid systems of fixed thermal insulators (e.g., walls) and fixed optical conductors (e.g., windows) [2]. This static disposition critically undermines energy performance; buildings aim to maintain a constant indoor environment, but cannot tune material properties to quickly address hourly, diurnal, and seasonal fluctuations in exterior temperature, daylight availability, and radiative solar intensity [3,4]. The development of active building facades, capable of achieving on-demand responses to these solar fluctuations, has emerged as an important scientific and engineering challenge [5].

Conventional mechanisms to control light transmission through the building facade are generally either low-resolution, impractical, or expensive. Most conventionally, buildings actively shade through manual or automated blinds, controlled on the interior side of the facade [6]. Related mechanical proof-of-concept systems have also been reported, including rotating fritting structures [7], bending elements [8], and active microscopic and milliscopic daylight-regulating louvers [9,10], each able to modulate shading density. Unfortunately, some of these mechanical systems are low-resolution, rigid, and prone to failure, and have only been

* Corresponding author. Department of Mechanical and Industrial Engineering, University of Toronto; 5 King's College Road, Toronto, Ontario, M5S 3G8, Canada.

E-mail address: raphael.kay@mail.utoronto.ca (R. Kay).

<https://doi.org/10.1016/j.jobee.2021.103942>

Received 18 July 2021; Received in revised form 13 December 2021; Accepted 22 December 2021

Available online 25 December 2021

2352-7102/© 2021 Elsevier Ltd. All rights reserved.

implemented within a handful of buildings to date [1]. Stimulus-responsive mechanisms have also been proposed for dynamic shading applications, where local environmental changes, rather than mechanical actuations, drive material configuration. For instance, moisture uptake in hygroscopic materials, driven by vapor pressure gradients, can cause a macroscopic change in material structure [11–13]. Similar efforts have been established to develop thermo- and photochromics, which modulate optical transmission in response to temperature and light intensity [14–16]. Despite the potential to achieve local actuation without a supplied energy source, the inability to decouple these material responses from their dedicated environmental stimuli limits applicability within real-life building environments [15]. Electrochromic devices have also been developed for buildings, where a controllable electric potential can be leveraged to modulate optical transparency [15,17,18]. While the functional performance of these systems has improved drastically over the years, their manufacturing remains costly and complex [3,18].

In this paper, we introduce an entirely new chromogenic platform, leveraging the pressure-induced emergence of air bubbles to control optical transmission within a confined multifluidic building layer. Based on well-established fluid-dynamic instabilities, we demonstrate systematic digital control over bubble morphology and bubble size. And we show that dynamic air bubble injections can be used to modulate visible light transmission, near-infrared light transmission, and radiative heat flow to regulate solar ingress in the built environment.

2. Bubble self-assembly background

When a fluid of lower viscosity is forced with pressure into a second fluid of higher viscosity, the interface between fluids becomes unstable [19]. While first observed in oil fields, where the interface between water and oil is susceptible to bifurcation and branching during oil extraction, this nonlinear fluidic phenomenon has fascinated physicists and mathematicians for nearly a century [19,20]. Known as viscous fingering, this instability is most commonly studied within quasi-two-dimensional venues, known as Hele-Shaw cells, where one fluid is introduced into the next between two closely-spaced rigid plates [21–24].

As first demonstrated by Saffman and Taylor [19], the interface between the injected ‘guest’ fluid (e.g., air) and displaced ‘host’ fluid within a Hele-Shaw cell will become unstable, and is susceptible to fractal-like branching, if the amplification factor of a branch width, $a_i > 0$, for

$$a_i = 3V\Delta n - \sigma\left(\frac{\pi b}{\lambda}\right)^2 \tag{1}$$

Here, flow in the vertical plane due to buoyant forces is assumed to be negligible, V is the velocity of the fluid bubble (e.g., air) at

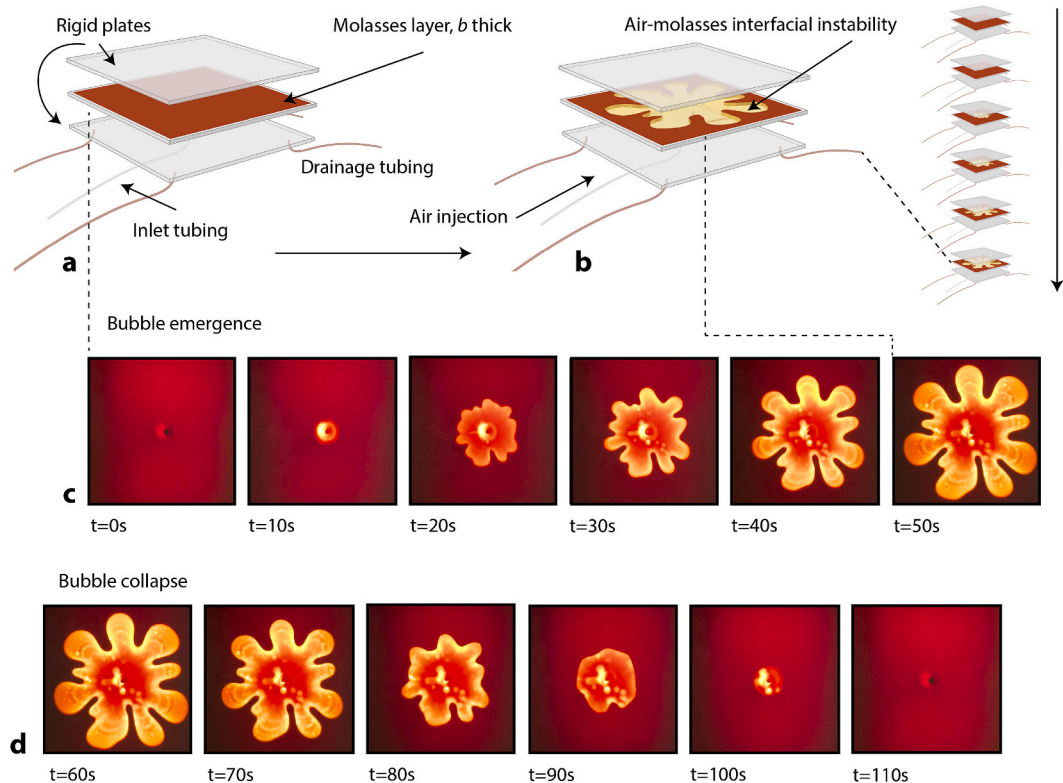


Fig. 1. (a) Hele-Shaw cell filled with viscous molasses. (b) Hele-Shaw cell with radial bubble following pressurized air injection over time. (c) Images of radial bubble emergence and (d) collapse sequence over time within Hele-Shaw cell.

the interface, $\Delta n = n_h - n_g$, n_h is the host fluid viscosity, n_g is the invading guest fluid (e.g., air) viscosity, b is the gap between plates, σ is the interfacial surface tension, and λ is the finger width of the instability [25]. Simply, an invading fluid bubble will bifurcate and form branches if the left-hand term is larger than the right-hand term – e.g., if the invading guest fluid is injected fast enough to overcome surface tension.

3. Materials and methods

Hele-Shaw cells were fabricated comprising two rigid PMMA plates ($30 \times 30 \times 0.6 \text{ cm}^3$). Plates were sealed at the seams using a 1-mm-thick double-sided elastomer adhesive (3M), creating a 1-mm-thick planar space for fluid flow. Hele-Shaw cells were designed with both a central and boundary inlet. For the former case, we milled an inlet port at the center of, and four outlet ports at the corners of, the top PMMA plate. For the latter case, we milled an inlet port along one boundary of, and two outlet ports at the opposite corner boundaries of, the top PMMA plate. Luer locks were adhered to the inlet ports, and connected to PVC tubing (1/4" I.D. x 3/8" O.D.). We fed the tubing to a NE-1010 digital syringe pump, to control flow rate and flow direction. All outlet ports were left open to the atmosphere, and we filled the Hele-Shaw cell with a highly-viscous opaque molasses liquid (Fig. 1a), as an inexpensive, widely-available, and non-toxic fluid.

To generate reversible air bubbles, we introduced air into the molasses layer confined within the Hele-Shaw cell at a controlled speed (25 mL/min) (Fig. 1b). The air first compressed, before rapidly self-assembling within the cell – at which point volume was estimated to be constant, and therefore pressure was assumed to be constant. As air bubbles displaced the molasses layer, light transmission increased through the cell. Optical transmission spectra, through both the visible and near-infrared regions, were measured with a Lambda 1050 Spectrophotometer (three-detector module). Time-dependent visible light intensity was measured behind the cell with an Extech HD450 Light Meter Datalogger. And time-dependent temperature was measured behind the cell with a k-type thermocouple. Bubbles were reversibly collapsed by reversing the direction of flow on the syringe pump.

By assuming Darcy Flow within this constant field (i.e., instantaneous flow rate is proportional to the pressure gradient, $q \propto \nabla P$), we were able to assume mathematical analogy to an electromotive model, where field strength is proportional to the gradient of electrostatic potential, $E \propto \nabla V$. Static, steady-state, potential flow for two flow-field configurations (i.e., isotropic and anisotropic) was accordingly approximated by calculating an electric potential field (MATLAB, code adapted from Ref. [26]), where each inlet was prescribed a charge of +1 and each outlet a charge of -1.

4. Results

4.1. Reversible bubble injection

We injected an air bubble into an opaque host phase (molasses) confined within a Hele-Shaw cell (Fig. 1c). Due to the high Δn between air and molasses, the interface became unstable, and the bubble bifurcated and branched as it grew. We subsequently

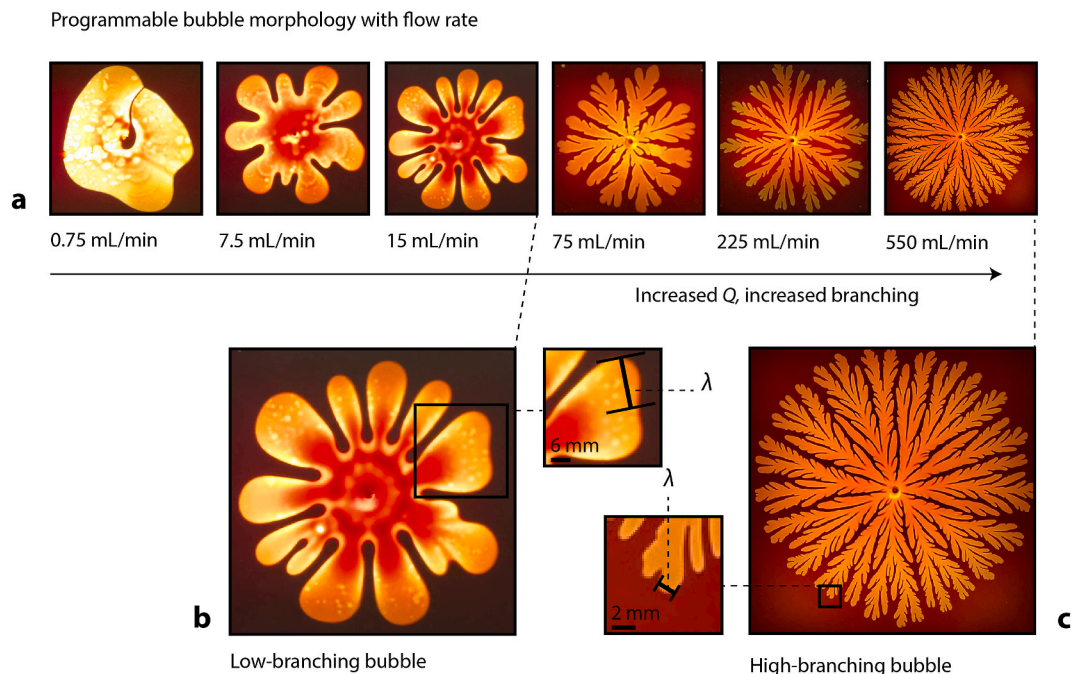


Fig. 2. Programmable bubble morphology with injection flow rate. (a) Different bubble morphologies following injection, where each air bubble was injected at a different constant rate. (b–c) Comparison of relative branch width between two bubbles injected at different rates (15 mL/min versus 550 mL/min).

collapsed the bubble by switching the direction of air flow to create negative pressure (Fig. 1d). This action also switched the direction of instability – the collapsing interface became stable as Δn turned negative – demonstrating stable reversibility over bubble growth. We repeated this emergence-collapse cycle, showing good consistency and repeatability ($n > 50$ cycles).

4.2. Tuning bubble morphology with injection rate

We injected air bubbles into an opaque molasses phase confined within a Hele-Shaw cell at different constant flow rates, ranging from 0.75 to 550 mL/min (Fig. 2a). As the flow rate increased, the width of the branches decreased, as $3V\Delta n$ grew [19], as can be verified in the well-established derivation of equation (1) into equation (2) [19]. By indirectly tuning V through control over injection flow rate of air, we can control bubble morphology within the cell.

$$\lambda = \pi b \sqrt{\frac{\sigma}{V\Delta n}} \quad (2)$$

4.3. Tuning bubble morphology with flow field

Beyond this localized morphological control, we demonstrated control over global pattern morphology through the deliberate placement of inlet and outlet ports within a Hele-Shaw cell. The relative position of inlet and outlet ports, and the relative geometry of the confined cell, determines the static potential flow for the emerging bubble. In Fig. 3, we demonstrate relative morphology between a bubble emerging from a central injection port within a radially-isotropic flow field (Fig. 3a–b) and a bubble emerging from a boundary injection port within a directionally-biased anisotropic flow field (Fig. 3c and d). While the bubble expands radially in the former case, the bubble expands unidirectionally in the latter case. We speculate that there might be functional benefits to each of these design scenarios – most obviously, a boundary inlet enables better concealment of injection tubing over a central inlet.

4.4. Adaptive and reversible modulation of visible light transmission

We injected and subsequently collapsed an air bubble within our Hele-Shaw cell. Air bubbles displaced a significant volume of the molasses layer, greatly decreasing the cross-sectional path length of molasses through which light was required to travel. We characterized the local change in visible light transmission through the cell, as a function of wavelength, for a fluidic region with and without an air bubble. For cross-sectional regions within the Hele-Shaw cell occupied by an air bubble, the average transmissivity across the visible region of the electromagnetic spectrum was measured using a spectrophotometer to be roughly 35.3% (Fig. 4b). Alternatively, for cross-sectional regions within the Hele-Shaw cell unoccupied by an air bubble (i.e., occupied completely by molasses), the average transmissivity across the visible region of the electromagnetic spectrum was measured using a spectrophotometer to be roughly 4.3% (Fig. 4b).

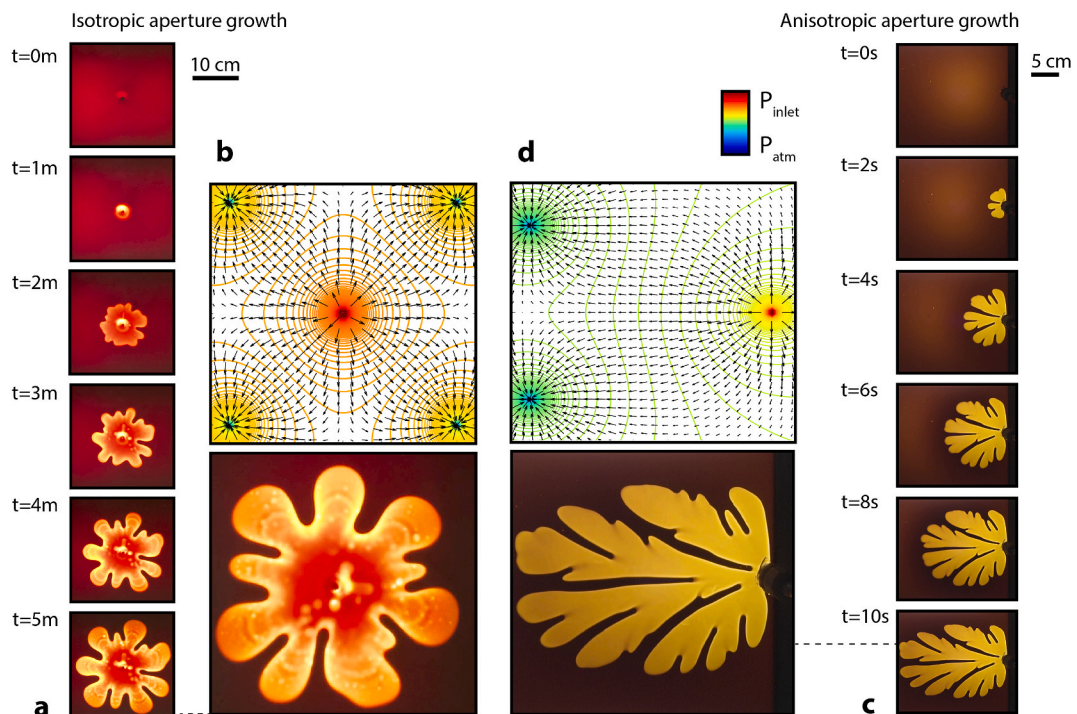


Fig. 3. The effect of isotropic versus anisotropic flow field on bubble morphology. (a–b) Radially-isotropic potential flow from central inlet to equidistant boundary outlets causes radial bubble formation. (c–d) Directionally-anisotropic potential flow from boundary inlet to boundary outlets causes anisotropic, directionally-biased bubble formation.

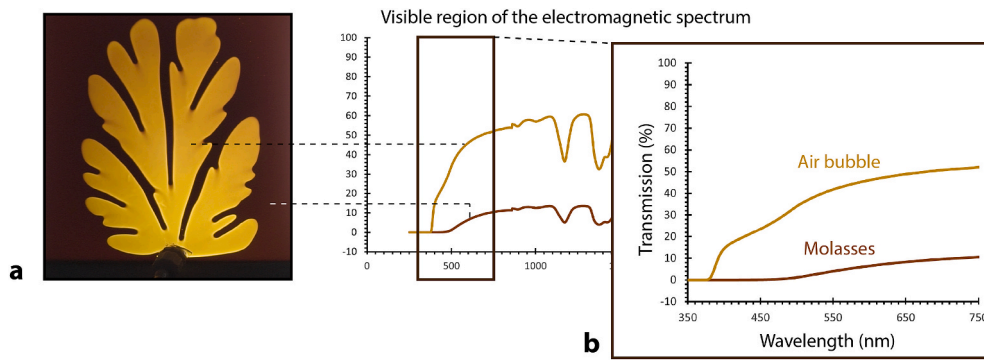


Fig. 4. Local visible light transmission changes with the injection of an air bubble. (a) Air bubble fully expanded within molasses-filled Hele-Shaw cell. (b) Light transmission within the visible region of the electromagnetic spectrum for both the molasses-filled Hele-Shaw layer with (air bubble) and without (molasses) air displacement. Average transmissivities for air bubble and molasses Hele-Shaw cell regions across the visible portion of the electromagnetic spectrum (350–750 nm) are 35.3% and 4.5%, respectively.

We then characterized the global change in visible light transmission through the entire cell, as a function of cell size across its emergence and collapse (Fig. 5a). We developed a simple ‘shoebox’ model ($30 \times 30 \times 30 \text{ cm}^3$) to control for, and within which to measure, interior light intensity. We replaced a portion of one of the six exterior facades of the model with our fluidic cell, and illuminated the model room from the exterior using a LED light bulb (providing 300 lux into the space with the panel removed) (Fig. 5b). Interior light intensity was measured from the back of this room, registering a baseline value of 15 lux prior to bubble injection (Fig. 5c), corresponding to a baseline transmissivity value of 4.5% (15/300 lux) within the visible spectrum. Air was injected at a constant rate of 25 mL/min and we measured both interior light intensity (Fig. 5c) and air bubble area fraction (Fig. 5d) over time. By dividing measured interior light intensity by measured incident light intensity (300 lux), we were able to characterize transmissivity through the entire cell over time (Fig. 5e) – an important property for assessing the optical performance of adaptive glazing. We report good agreement between measured transmissivity (data points in Fig. 5e) and a theoretical prediction of transmissivity (dotted black line in Fig. 5e), calculated by taking the light transmission of the air bubble and molasses layer averaged across all visible wavelengths (350–750 nm, measured using spectrophotometry as 35.3% and 4.3%, respectively), weighted by their measured area fractions across injection. In simpler terms, this prediction entailed multiplying the measured area fraction of the air bubble by the transmissivity of the air bubble (0.353) and the measured area fraction of the molasses by the transmissivity of the molasses (0.043), and summing these products. As predicted, light transmission and transmissivity both increased as the size/area fraction of the bubble increased, and we showed that light intensity and transmissivity moved approximately linearly with bubble area fraction (Fig. 5f and g), to a maximum value of roughly 14%. In Fig. 5g, we compared measured transmissivity values (interior light intensity divided by incident light intensity) to our theoretical prediction, showing broad agreement.

4.5. Adaptive and reversible modulation of near-infrared light transmission, solar heat gain, and heat flow

Beyond describing changes to visible light transmission, we characterized the local change in near-infrared light transmission through the cell, as a function of wavelength, for a temporary air bubble injection (Fig. 6). Similar to the effect demonstrated in the visible region of the electromagnetic spectrum, air injection caused an increase in near-infrared light transmission (Fig. 6b). Both this increase in near-infrared light transmission, and the previously-demonstrated increase in visible light transmission, cause an increase in radiative heat flow across the Hele-Shaw cell. This change in radiative heat flow can be captured using a solar heat gain coefficient (SHGC),

$$SHGC = T_{sol} + A_{sol} \cdot N \quad (3)$$

Where T_{sol} is the total fractional solar transmittance of the glazing system (unitless), A_{sol} is the fractional solar absorbance of the glazing system (unitless), and N is the fraction of solar heat that flows inward following absorbance (unitless). Here, T_{sol} of a material can be computed as the solar irradiance received on the exterior surface of the material (Fig. 6c) at each wavelength multiplied by the material transmissivity at each wavelength, all divided by the total solar irradiance on the exterior surface of the material. If we presume that our Hele-Shaw cell is located on the exterior of a well-insulated window unit, we can assume solar heat gain through absorption and reemission, the second term of Equation (3), to be negligible. Accordingly, Equation (3) can be simplified such that the SHGC of a material is equal to the total solar transmittance of that material.

Using the transmissivity data in Fig. 6b, we calculated the SHGC of our Hele-Shaw cell cross-section with both an air bubble present and without, finding a SHGC of 43% and 7%, respectively. These SHGCs represent functional bounds to the performance of our system, where our cell prior to an air injection can transmit 7% of solar radiation and a cell after a maximum air injection covering 100% of the total area can transmit 43% of solar radiation. Using data on the area fraction of an air bubble over a complete injection and retraction sequence (demonstrated in Fig. 5a), we calculated the effective SHGC of the cell at each time step by multiplying the air bubble area fraction by 0.43 and the molasses area fraction by 0.07, and summing these components (Fig. 6d). Effective SHGC accordingly moved linearly with air bubble area fraction, increasing from 7% to 21% for a change in area fraction from 0 to 39% (Fig. 6e).

Effect of fluid cell opening on internal light intensity

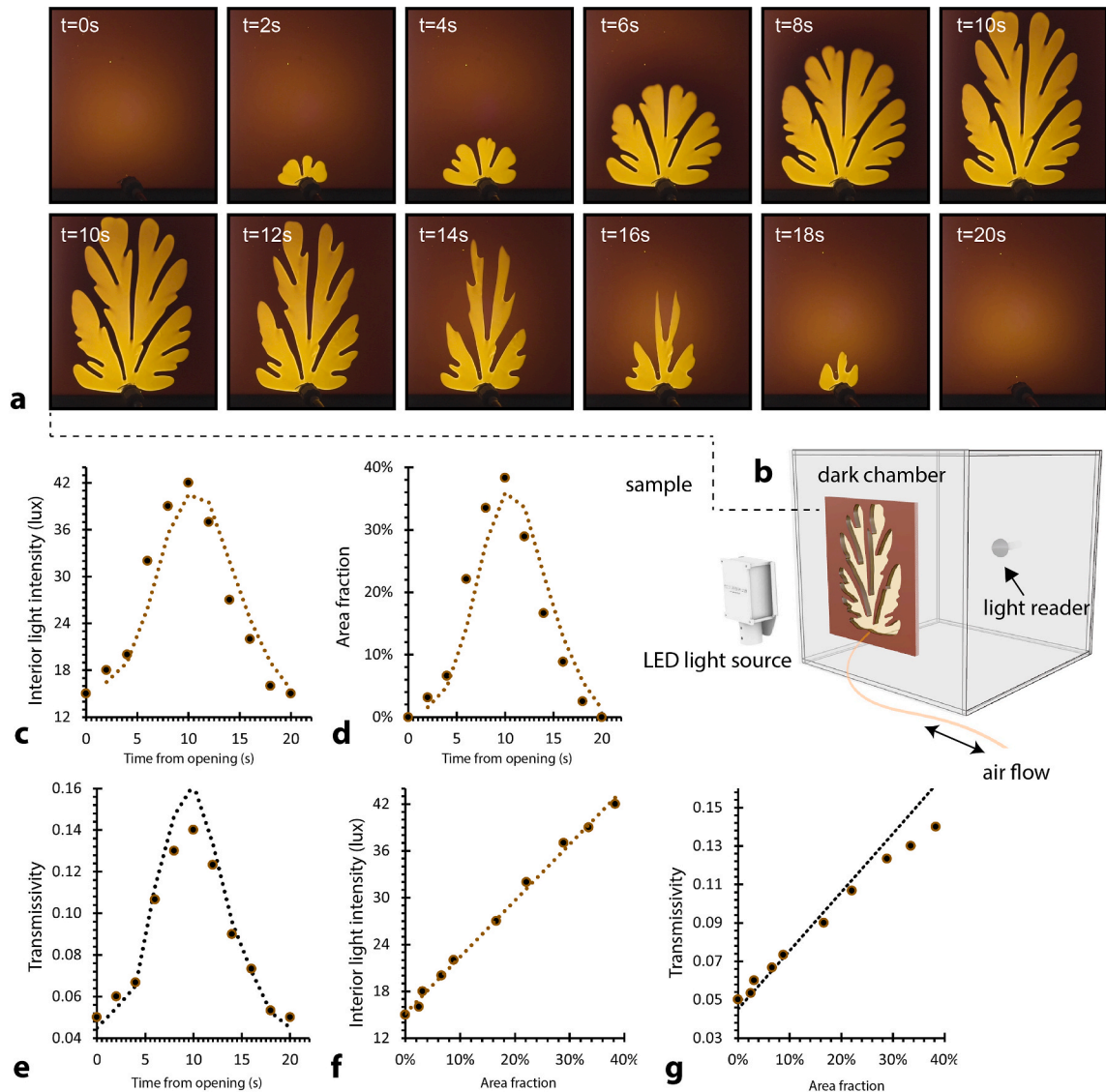


Fig. 5. Modulation of visible light transmission in a Hele-Shaw cell (a) Reversible injection and collapse of air bubble within Hele-Shaw cell. (b) Schematic illustrating experiment to measure interior light intensity. (c) Change in interior light intensity over injection time. Dotted brown line represents moving average. (d) Change in bubble area fraction over injection time. Dotted brown line represents moving average. (e) Change in cell transmissivity over time. Dotted black line represents theoretical transmissivity, calculated as the average visible transmission for air bubble and molasses fractional area components. (f–g) Interior light intensity and cell transmissivity move approximately linearly with bubble area fraction. Dotted brown line in (f) represents best fit linear trendline. Dotted black line in (g) represents theoretical transmissivity, calculated as described in (e). For simplicity, experiment illustrated in (b) conducted in the horizontal plane (setup rotated 90°). (For interpretation of the references to color in this figure legend, the reader is referred to the Web version of this article.)

To experimentally validate this result, we developed a similar ‘shoebox’ model as described in the preceding section ($30 \times 30 \times 30 \text{ cm}^3$), but removed four of the six walls to assess the effect of radiative heat transfer in a well-ventilated space (i.e., isolating radiative heat transfer) (Fig. 7b). To provide radiative energy, the cell was illuminated with a 50-W incandescent light bulb (Fig. 7b), allowing a thermocouple measuring the temperature of a PMMA sheet within the space to reach a thermal equilibrium (after 30 min) of 30°C prior to bubble injection (Fig. 7c, $t = 1 \text{ min}$). We then injected air at a constant rate of 25 mL/min for 10 s, injecting approximately 4 mL. As predicted, the temperature of the interior PMMA sheet began to increase after the air bubble was injected, reaching a new thermal equilibrium of 37°C after 9 min (Fig. 7c). Six minutes later, we collapsed the bubble, and observed a reversible radiative thermal effect, where the temperature of the interior sheet decreased back to below 30°C (Fig. 7c, $t = 27 \text{ min}$).

4.6. Motion-induced digital bubble response

To demonstrate the potential of this material system within a responsive building facade, we developed a digital feedback system to

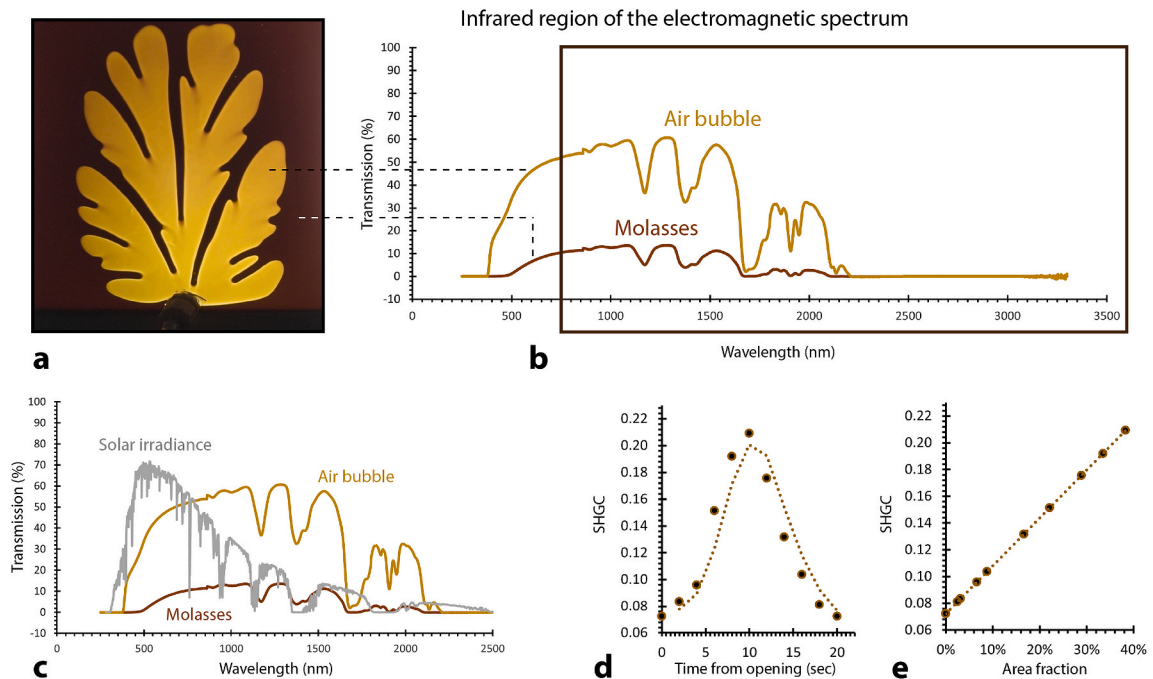


Fig. 6. Local near-infrared light transmission and solar heat gain changes with the injection of an air bubble. (a) Air bubble fully expanded within molasses-filled Hele-Shaw cell. (b) Light transmission within the near-infrared region of the electromagnetic spectrum for both the molasses-filled Hele-Shaw layer with (air bubble) and without (molasses) air displacement. (c) Light transmission data from (b) overlaid atop solar radiation spectrum on earth, where radiation values are represented in units along the y-axis of $50 \text{ W/m}^2/\text{nm}$ (data from National Renewable Energy Laboratory). Solar heat gain coefficient (SHGC) for air bubble and molasses region is 43% and 7%, respectively. (D) Effective SHGC of Hele-Shaw cell over time (same experiment as depicted in Fig. 5a), where effective SHGC is measured as the area-normalized SHGC of the air bubble and molasses regions of the cell. (E) SHGC therefore moves linearly with air bubble area fraction.

couple the electrical input of an ultrasonic distance sensor (Parallax 28015) to the electric output of a peristaltic pump (INTLLAB 12V). We programmed two distance thresholds, such that a hand wave within 10 cm of the cell-integrated sensor would drive the injection of an air bubble, and a hand wave between 10.1 cm and 30 cm from the cell would drive the collapse of that air bubble. This ultrasonic-fluidic feedback was demonstrated over several cycles – one of which is illustrated over a 12 s time period in Fig. 8.

4.7. Modelled building energy consumption

4.7.1. Simulation setup and control algorithm

To demonstrate the energy performance of our active fluid layer, we used a building energy modelling tool (EnergyPlus) to estimate the annual energy required for heating, cooling, and lighting a conventional office space locating in Toronto, Canada. In particular, we compared energy costs for conditioning the space when clad along its south face with (i) our switchable Hele-Shaw cell, (ii) a state-of-the-art electrochromic (EC) window, (iii) a dynamic roller shade (RS) interior to a double-glazed window, and (iv) a static low-emissivity control double-glazed window. The one-zone reference office, illustrated in Fig. 9a and described in detail in Ref. [27], is 3.6 m wide (E-W direction) and 8.2 m deep (N-S direction), with a south-facing window (window-to-wall ratio of 88%). For consistency, the operation of each of these three dynamic systems (i-iii) was simulated using a standard control algorithm, designed as a naïve energy minimizer, restricted to maintain a set illuminance of 300 lux across 50% of the model floor area during each occupied hour. Additionally, the algorithm restricted the over-lit area (defined as exceeding 3000 lux) to less than 10% of the model floor area.

The Hele-Shaw cell was modelled to switch between seven possible states, derived from the effective transmission spectra for a Hele-Shaw cell with air bubble area fractions between 0% and 60% (at 10% steps) (transmission spectra shown in Fig. 9b, left). This air bubble area fraction of 60% represents an upper functional limit that we observed in our physical experiments in square-shaped Hele-Shaw cells. The EC window was modelled to switch between four standard states (transmission spectra taken from a real market product, and shown in Fig. 9b, center). And, finally, the RS was modelled to switch between its two standard states (up and down), where the 'up' state corresponded to the transmission spectrum of a double-pane control window by itself (Fig. 9b, right). To account for building integration, the EC window and Hele-Shaw cell were modelled on the exterior, and the RS was modelled on the interior, of a standard double-pane window. This standard control window had a visible transmittance value of 81%, a SHGC of 71%, and a conductive heat transfer coefficient (U-value) of $1.81 \text{ W/m}^2\text{K}$. Our seven Hele-Shaw cell states (Fig. 9b, left), when combined with the standard control window, had visible transmittance values of 22, 19, 16, 13, 9, 7, and 4%, and SHGC values of 23, 20, 17, 14, 11, 9, and 6%, respectively.

For every hour in which the space was occupied, each available control state (defined in Fig. 9b for each dynamic system) was tested to satisfy the required illuminance and overlighting constraints (Fig. 10). For each material state meeting these constraints, solar

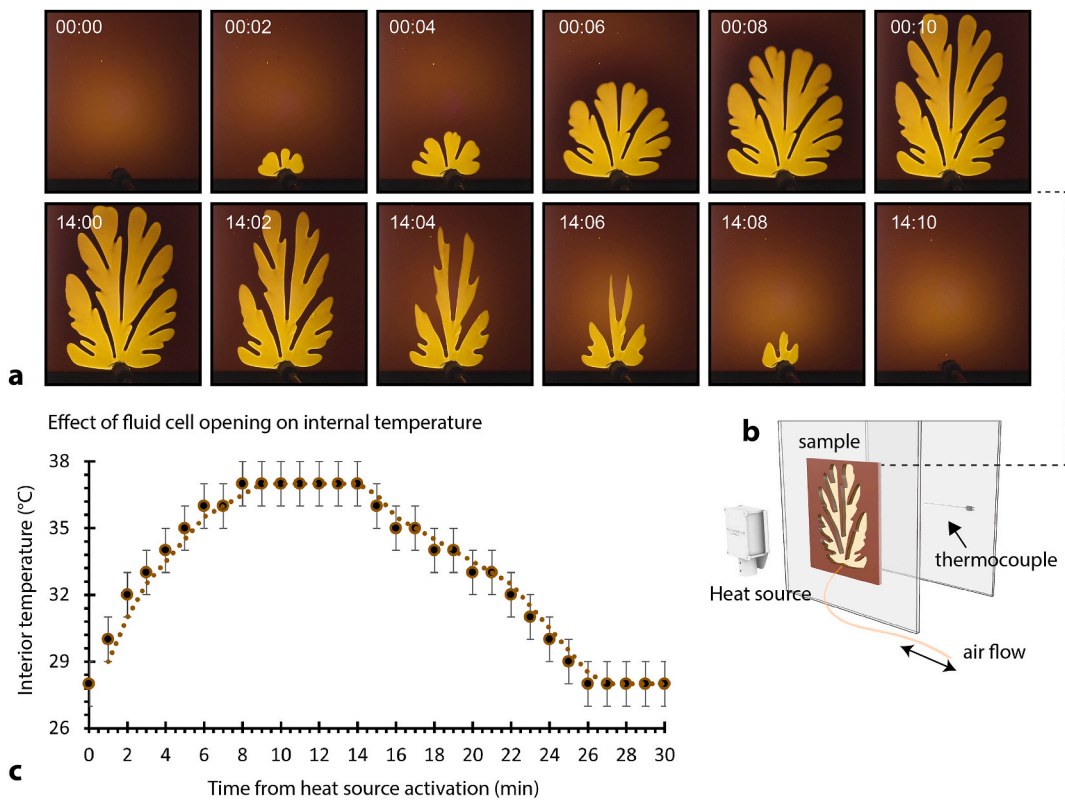


Fig. 7. Modulation of near-infrared light transmission in a Hele-Shaw cell. (a) Reversible injection and collapse of air bubble within Hele-Shaw cell. (b) Schematic illustrating experiment to measure interior temperature. (c) Change in interior temperature over time with air bubble injection and collapse. For simplicity, experiment illustrated in (b) conducted in the horizontal plane (setup rotated 90°).

Motion-driven digital bubble growth and collapse

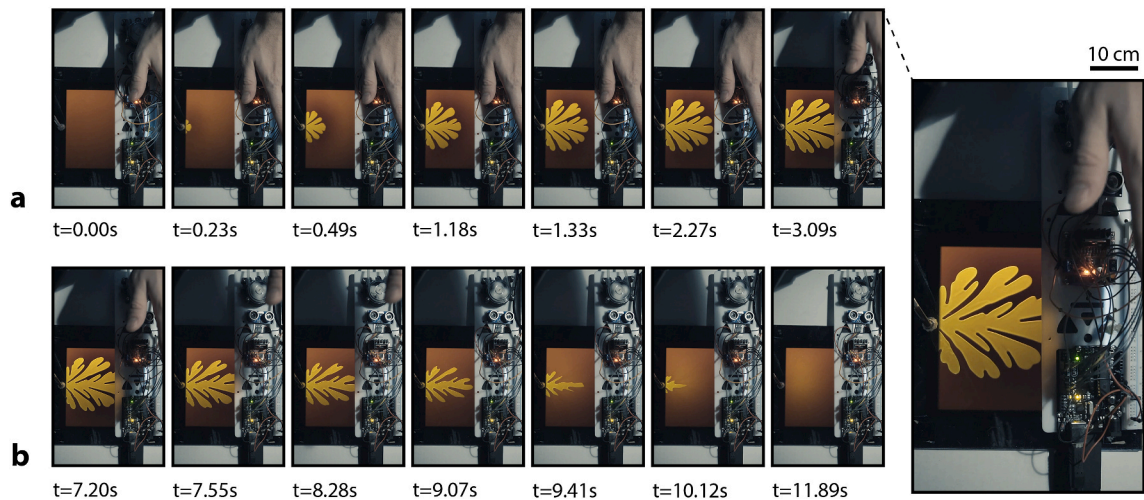


Fig. 8. Tunable ultrasonic detection can drive a proportional fluidic response. (a) Injection of air bubble proportional to the amount of time a hand is detected within the forward-growing distance threshold (0.1–10 cm). (b) Collapsing of air bubble proportional to the amount of time a hand is detected within the backward-growing distance threshold (10.1–30 cm).

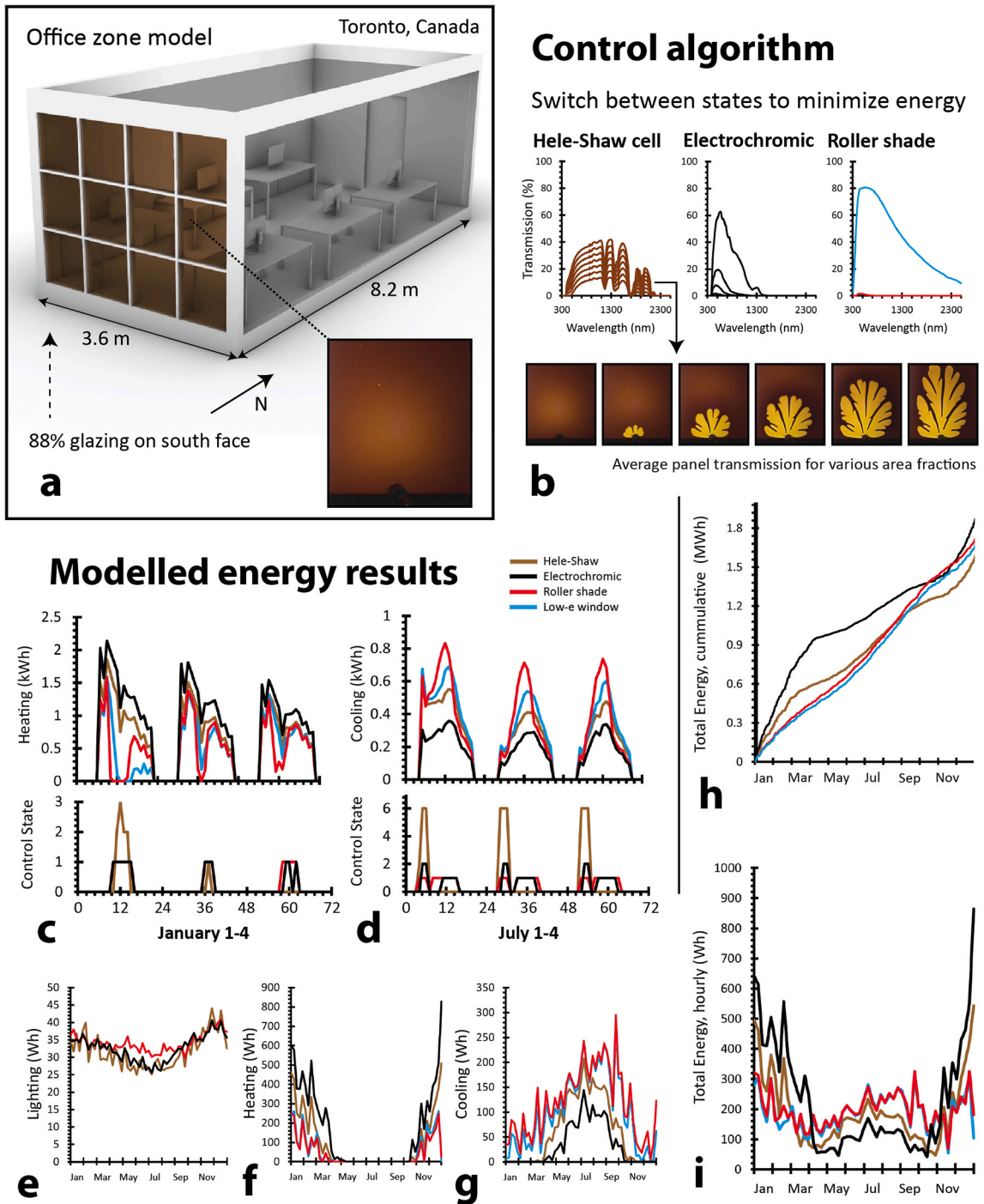


Fig. 9. Comparative energy performance of active Hele-Shaw cell. (a) Reference office model for energy simulations. Note: roof and walls are translucent only for illustrative clarity, and were modelled as opaque elements in simulation. (b) Available control states for dynamic switching of Hele-Shaw cell, EC window, and RS. (c-d) Simulated hourly heating and cooling loads across typical 72-h winter and summer periods, respectively, for office space clad in Hele-Shaw cell, EC window, RS, and static control window. Bottom charts show control states for three dynamic systems across identical 72-h intervals, where 0 represents maximum transmission state (minimum transmission state for Hele-Shaw cell is 6, EC window is 3, RS is 1). (e-g) Simulated average hourly heating, cooling, and electric lighting energy usage, averaged across weekly time periods, for office space clad in Hele-Shaw cell, EC window, RS, and static control window. (h) Total simulated cumulative energy usage for Hele-Shaw cell, EC window, RS, and control window. (i) Average hourly energy (heating, cooling, and lighting) usage for Hele-Shaw cell, EC window, RS, and control window, averaged across weekly time periods.

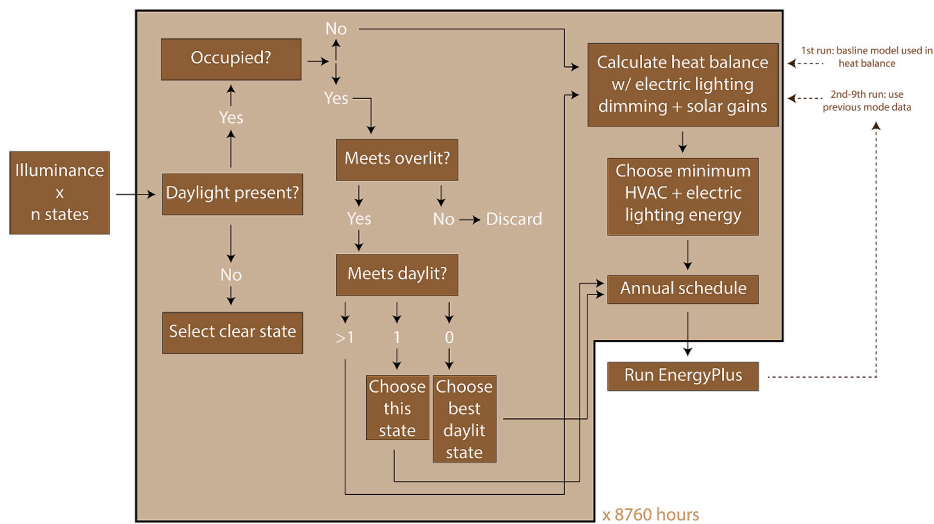


Fig. 10. State selection control algorithm for dynamic operation of all multistate facade systems (Hele-Shaw cell, EC window, and RS). >1, 1, and 0 refer to the number of states that meet both the overlit and daylight criteria.

heat gain and electric lighting utilization were calculated. Once the acceptable daylight-driven requirements were met, a heat balance was calculated at each hour based on thermal model outputs for internal heating loads (occupants, lights, equipment) and external heating loads (ventilation, solar heat gains, conduction). Of all calculated material states, the state that minimized total energy (combined heating, cooling, and lighting) was selected. Because the underlying thermal models are transient in nature (i.e., each timestep influences the next), the control algorithm was iterated many times until annual energy results stabilized. This allowed a near-optimal control system to be achieved. The state-selection algorithm for all dynamic systems is illustrated in Fig. 10, and all additional simulation details are provided in Table 1.

4.7.2. Simulation results

In simulation, we found that the dynamic operation of our Hele-Shaw cell could reduce total annual operation energy usage in our office space by 16%, 7%, and 4% over EC, RS, and static glazing systems, respectively (Fig. 9h). The roller shade and static control window followed similar temporal consumption trends (Fig. 9e-i), requiring, in comparative terms, much more energy to achieve cooling than heating. Conversely, the EC window and Hele-Shaw cell followed similar temporal consumption trends (Fig. 9e-i), requiring, in comparative terms, much more energy to achieve heating than cooling. Despite this consumption trend similarity, our Hele-Shaw cell required much less energy than did the EC window to heat the indoor space (Fig. 9f), resulting in reduced energy consumption compared with the EC system. This performance difference was likely achieved by the fact that our Hele-Shaw system can

Table 1
Simulation parameters.

| Parameter | Modelled property |
|--|--|
| Zone volume (m ³) | 100.39 |
| Zone floor area (m ²) | 29.52 |
| WWR of south facade (%) | 88 |
| Fresh air supply (m ³ /s/person) | 0.0125 |
| Air infiltration (air exchanges per hour) | 0.1 |
| Occupancy schedule | Office, 5 days per week, from [28] |
| Occupant density (m ² /person) | 0.0538 |
| Heating setpoint while occupied (°C) | 21.0 |
| Cooling setpoint while occupied (°C) | 24.0 |
| Heating setpoint while unoccupied (°C) | 15.6 |
| Cooling setpoint while unoccupied (°C) | 26.7 |
| Heating system efficiency (%) | 80 |
| Cooling system coefficient of performance | 3.2 |
| Sensible heat recovery efficiency (%) | 70 |
| Latent heat recovery efficiency (%) | 65 |
| Lighting power (W/m ²) | 3.4, 7:00–19:00 with dimming |
| Indoor material properties | IES LM-83 convention [30] |
| Thermal definition of all non-exterior walls, floors, ceilings | Adiabatic |
| Opaque walls U-value (W/m ² K) | 0.472 |
| Heat generation rate of all occupants (W) | 125 |
| Equipment power (W/m ²) | 5 |
| Equipment operation schedule | From National Energy Code of Canada for Buildings [28] |

admit much more near-infrared light for each unit of admitted visible light (compare spectral distributions in Fig. 9b), enabling higher solar heat gains within a given limit of overlighting. We found that electric lighting consumption played a smaller role in total energy consumption, and that all systems performed comparatively across the year (Fig. 9e).

4.7.3. Operational energy cost calculation

To assess the feasibility of building integration, we estimated the energy required to optimally operate our fluidic Hele-Shaw cell across the year. We calculated the annual operational energy as the energy required for a typical peristaltic pump to inject or retract an air bubble within a 0.25 m^2 panel in our experiments ($5 \text{ W} * 4 \text{ s}$), multiplied by the number of times an injection or retraction occurred in our annual energy simulation (1630), multiplied by the number of 0.25 m^2 panels needed to cover the south-face glazing (9.5 m^2) of our one-zone simulation space (38). We obtained an estimated operational energy cost of 0.344 kWh (0.036 kWh/m^2), or about 0.12% of the energy that our dynamic Hele-Shaw system could save over an EC window in our simulation (303.5 kWh). This result importantly suggests that our Hele-Shaw cell might have only a negligible operational energy cost, validating building integration feasibility.

4.8. Implementation cost and breakeven point

Our Hele-Shaw cell can be fabricated using off-the-shelf PMMA sheets and molasses, and can be operated using simple electronics with a low required energy supply (0.036 kWh/m^2). In our experiments, these Hele-Shaw systems, including all fluidic, casing, and electronic components, were built for approximately $\$25 \text{ USD/m}^2$.

Using this unit cost and the reference office model introduced in Fig. 9a, we can assume an implementation (breakeven) cost of about $\$380 \text{ USD}$ to completely clad the 9.5 m^2 south-facing glazing array ($\$25 \text{ USD/m}^2$ for the device and $\$15 \text{ USD/m}^2$ for the fastening system required to connect the Hele-Shaw cell to an existing double-glazed unit). Our energy models provided an estimate of the energy that our Hele-Shaw device could reduce annually over a static double-glazed window (67.6 kWh , accounting for the 0.344 kWh for annual operation). Assuming that all heating, cooling, and lighting loads can be supplied by electricity, we used the mid-peak cost of electricity in Toronto, Canada ($\$0.893 \text{ USD/kWh}$, 2021) to calculate the breakeven point for our Hele-Shaw cell system. It was found that our Hele-Shaw system can be expected to save approximately $\$60.37 \text{ USD/year}$ in electricity costs, paying back the $\$380 \text{ USD}$ implementation cost in just over 6 years.

5. Discussion

We developed a methodology to translate well-established nonlinear fluid dynamics to responsive building facades in architecture. We demonstrated shape- and size-tunable bubble injections to modulate both visible light transmission and near-infrared heat gain within a mock-building interface, and achieved reversibility over multiple cycles. We then simulated the energetic performance of our system within a prototypical office model, and found that the dynamic operation of our Hele-Shaw system (switching between air injection states that cover 0–60% of the model's south-facing facade) could reduce annual energy consumption by up to 16% over a state-of-the-art electrochromic window. Our experimental and modelled results suggest building integration feasibility, with the potential for substantial improvements to architectural energy efficiency.

5.1. Future considerations

Because the interface between air and the opaque host phase (in this case, molasses) is highly unstable, the branched pattern morphology of the injected bubble represents only a meta-stable state, where the resistance to flow of the molasses phase enables longer-term (minutes-hours) pattern stability. In thermodynamic terms, decay of the branching state is inevitable over time, but the time-scale of branch-decay for these specific fluids must be better understood in order to assess the limitations in long-term patterning and light transmission within a Hele-Shaw cell.

Similarly, while buoyant forces had a negligible impact on bubble morphology for injections within vertically-oriented cells ($t = 40 \text{ min}$), the decay of bubble morphology may be amplified by gravitationally-induced forces arising from the difference in density between host-molasses and guest-air phases. Future work might explore multiphase systems with fluids (liquids in particular) of the same density.

In an architectural context, the system described here can only partially control visible light transmission (visible light transmissivity ranges between 4 and 35%, with low specular transmission). This property is unattractive in modern building facades, where views to the outdoors are universally expected, achieved through high specular transmissivity in the visible region of the electromagnetic spectrum. From a design point of view, we speculate that, by decreasing the flow rate of the injected air bubble and increasing the hydrophobicity of the inner Hele-Shaw cell surface, we might achieve increased displacement of the host phase (i.e., increased surface wetting by the air phase). This effect, explained by Bretherton [29], would result in a decreased molasses path length through which light would be required to travel, increasing the maximum light transmissivity, and specular light transmissivity, through the cell.

Alternatively, rather than as a replacement for traditional glazing, we envision that the demonstrated fluidic control might be desirable along both traditionally-opaque vertical (e.g., walls) and horizontal (e.g., rooves) elements within buildings – where visual clarity is not a necessity, but tunable control over visible and near-infrared light transmission remains critical for energy efficiency. In broad terms, we imagine that buildings might be entirely encapsulated by fluidic layers, enabling an improved spatial resolution of optical properties, rather than the stubborn paradigm of fixed transmission elements (windows) and fixed insulating elements (walls).

Importantly, we also note that the mechanism introduced here is generalizable. Air can be injected within a range of host liquid chemistries, where the viscosity and transmissivity of the host liquid can be selected to control the lifetime and rate of descent of an air

bubble and the range of optical transparency of the Hele-Shaw panel.

Finally, we suspect that the scope of this work can far exceed energy-efficient building design. Because the morphology of air bubbles can be tuned using digital control, we imagine that large, independently-addressable, multicell arrays might be easily developed to provide visual feedback through dynamic patterning. Accordingly, such a system could be applied across both soft and hard material interfaces, with possible applications for active color change and camouflage in wearables, sensors, communication technologies, and vehicles.

6. Conclusions

This paper describes a multifluidic interface for achieving reversible injections of self-organizing air bubbles. Through digitally-controlled fluidic actuation, we demonstrate tunability over both measured visible and near-infrared light transmission, with architectural implications for both interior daylighting and solar heat gain. This work represents an early exploration into multifluidic chromogenic building facades, and we speculate that its future incarnations might enable more advanced material responses in architecture, and elsewhere.

Author contributions

Conceptualization: RK, KN. Methodology: RK, KN, CK, NH. Physical experimentation: RK, KN. Simulation design and implementation: JAJ. Visualization: RK. Electronic system design: KN. Funding acquisition: BDH. Writing – original draft: RK. Writing – review and editing: RK, CK, JAJ, NH, BDH.

Funding

Canadian Foundation for Innovation (CFI) #31799 (BDH).

Percy Edward Hart Professorship, University of Toronto (BDH).

RK was supported by a Canada Graduate Scholarship, a C.W. Bowman Graduate Scholarship, and a Bert Wasmund Graduate Fellowship.

Declaration of competing interest

The authors declare that they have no known competing financial interests or personal relationships that could have appeared to influence the work reported in this paper.

Data availability statement

No datasets were generated or analyzed during the current study. All data can be made available by the authors upon request.

Acknowledgements

We thank David Correa for his time reviewing the manuscript.

References

- [1] R.C.G.M. Loonen, M. Trčka, D. Cóstola, et al., Climate adaptive building shells: state-of-the-art and future challenges, *Renew. Sustain. Energy Rev.* 25 (2013) 483–493, <https://doi.org/10.1016/j.rser.2013.04.016>.
- [2] S. Craig, J. Grinham, Breathing walls: the design of porous materials for heat exchange and decentralized ventilation, *Energy Build.* 149 (2017) 246–259, <https://doi.org/10.1016/j.enbuild.2017.05.036>.
- [3] Y. Wang, E.L. Rønnerstrom, D.J. Milliron, Switchable materials for smart windows, *Ann. Rev. Chem. Biomol. Eng.* 7 (2016) 283–304, <https://doi.org/10.1146/annurev-chembioeng-080615-034647>, 2016/03/30.
- [4] H. Khandelwal, A.P.H.J. Schenning, M.G. Debije, Infrared regulating smart window based on organic materials, *Adv. Energy Mater.* 7 (2017), 1602209, <https://doi.org/10.1002/aenm.201602209>.
- [5] W.J. Hee, M.A. Alghoul, B. Bakhtyar, et al., The role of window glazing on daylighting and energy saving in buildings, *Renew. Sustain. Energy Rev.* 42 (2015) 323–343, <https://doi.org/10.1016/j.rser.2014.09.020>.
- [6] M. Konstantoglou, A. Tsangrassoulis, Dynamic operation of daylighting and shading systems: a literature review, *Renew. Sustain. Energy Rev.* 60 (2016) 268–283, <https://doi.org/10.1016/j.rser.2015.12.246>.
- [7] Z. Drozdowski, S. Gupta, Adaptive fritting as case exploration for adaptivity in architecture, in: *Proceedings Of the 29th Annual Conference Of the Association For Computer Aided Design In Architecture* Chicago, 2009, pp. 105–109, Illinois, October 22–25.
- [8] J. Lienhard, S. Schleicher, S. Poppinga, et al., Flectofin: a hingeless flapping mechanism inspired by nature, *Bioinspiration Biomimetics* 6 (2011), 045001, <https://doi.org/10.1088/1748-3182/6/4/045001>.
- [9] D. Park, P. Kim, J. Alvarenga, et al., Dynamic daylight control system implementing thin cast arrays of polydimethylsiloxane-based millimeter-scale transparent louvers, *Build. Environ.* 82 (2014) 87–96, <https://doi.org/10.1016/j.buildenv.2014.07.016>.
- [10] V. Viereck, J. Ackermann, Q. Li, et al., Sun glasses for buildings based on micro mirror arrays: technology, control by networked sensors and scaling potential, in: *2008 5th International Conference on Networked Sensing Systems*, 2008, pp. 135–139, 17–19 June 2008.
- [11] D.M. Wood, D. Correa, O.D. Krieg, et al., Material computation—4D timber construction—towards building-scale hygroscopic actuated, self-constructing timber surfaces, *Int. J. Architect. Comput.* 14 (2016) 49–62, <https://doi.org/10.1177/1478077115625522>.
- [12] S. Reichert, A. Menges, D. Correa, Meteorosensitive architecture: biomimetic building skins based on materially embedded and hygroscopically enabled responsiveness, *Comput. Aided Des.* 60 (2015) 50–69, <https://doi.org/10.1016/j.cad.2014.02.010>.
- [13] S. Poppinga, C. Zollfrank, O. Prucker, et al., Toward a new generation of smart biomimetic actuators for architecture, *Adv. Mater.* 30 (2018), 1703653, <https://doi.org/10.1002/adma.201703653>.

- [14] C.G. Granqvist, Chromogenic materials for transmittance control of large-area windows, *Crit. Rev. Solid State Mater. Sci.* 16 (1990) 291–308, <https://doi.org/10.1080/10408439008242184>.
- [15] C.M. Lampert, Chromogenic smart materials, *Mater. Today* 7 (2004) 28–35, [https://doi.org/10.1016/S1369-7021\(04\)00123-3](https://doi.org/10.1016/S1369-7021(04)00123-3).
- [16] C.G. Granqvist, P.C. Lansåker, N.R. Mlyuka, et al., Progress in chromogenics: new results for electrochromic and thermochromic materials and devices, *Sol. Energy Mater. Sol. Cell.* 93 (2009) 2032–2039, <https://doi.org/10.1016/j.solmat.2009.02.026>.
- [17] D. Cupelli, F.P. Nicoletta, S. Manfredi, et al., Electrically switchable chromogenic materials for external glazing, *Sol. Energy Mater. Sol. Cell.* 93 (2009) 329–333, <https://doi.org/10.1016/j.solmat.2008.11.010>.
- [18] E.S. Lee, D.L. DiBartolomeo, Application issues for large-area electrochromic windows in commercial buildings, *Sol. Energy Mater. Sol. Cell.* 71 (2002) 465–491, [https://doi.org/10.1016/S0927-0248\(01\)00101-5](https://doi.org/10.1016/S0927-0248(01)00101-5).
- [19] P.G. Saffman, F.R.S. Sir Geoffrey Taylor, The penetration of a fluid into a porous medium or Hele-Shaw cell containing a more viscous liquid, in: P. Pelcé (Ed.), *Dynamics of Curved Fronts*, Academic Press, San Diego, 1958, pp. 155–174.
- [20] S. Hill, P. Fi, Channeling in packed columns, *Chem. Eng. Sci.* 1 (1952) 247–253, [https://doi.org/10.1016/0009-2509\(52\)87017-4](https://doi.org/10.1016/0009-2509(52)87017-4).
- [21] D.A. Kessler, J. Koplik, H. Levine, Pattern selection in fingered growth phenomena, *Adv. Phys.* 37 (1988), 255, <https://doi.org/10.1080/00018738800101379>.
- [22] I. Bischofberger, R. Ramachandran, S.R. Nagel, Fingering versus stability in the limit of zero interfacial tension, *Nat. Commun.* 5 (2014), 5265, <https://doi.org/10.1038/ncomms6265>.
- [23] I. Bischofberger, S.R. Nagel, Fluid instabilities that mimic animal growth, *Phys. Today* 69 (2016) 70–71.
- [24] I. Bischofberger, R. Ramachandran, S.R. Nagel, An island of stability in a sea of fingers: emergent global features of the viscous-flow instability, *Soft Matter* 11 (2015) 7428–7432, <https://doi.org/10.1039/C5SM00943J>, 10.1039/C5SM00943J.
- [25] P.G. Saffman, G.I. Taylor, The penetration of a fluid into a porous medium or Hele-Shaw cell containing a more viscous liquid, in: *Proceedings of the Royal Society of London Series A Mathematical and Physical Sciences*, 245, 1958, pp. 312–329, <https://doi.org/10.1098/rspa.1958.0085>.
- [26] Donadio L. Electric potential and electric field. https://www.youtube.com/watch?v=oE9D3fLYKsg&ab_channel=lorenzodonadio2016.
- [27] C.F. Reinhart, J.A. Jakubiec, D. Ibarra, Definition of a reference office for standardized evaluations of dynamic façade and lighting technologies. In *Proceedings of BS2013*, in: 13th Conference of International Building Performance Simulation Association, Chambéry, France, 28, 2013, pp. 3645–3652. August 26.
- [28] *National Energy Code of Canada for Buildings*, 2017.
- [29] F.P. Bretherton, The motion of long bubbles in tubes, *J. Fluid Mech.* 10 (1961) 166–188, <https://doi.org/10.1017/S0022112061000160>, 2006/03/28.
- [30] I. LM, IES Daylight Metrics Committee, Approved method: IES spatial Daylight autonomy (sDA) and annual sunlight exposure (ASE), *Illum. Eng. Soc.* (2013).